

Penalties From 2D Grating Coupler Induced Polarization Crosstalk in Silicon Photonic Coherent Transceivers

Galina Georgieva¹, *Student Member, IEEE*, Matheus Sena², *Member, IEEE*, Pascal M. Seiler¹,
Klaus Petermann¹, *Life Fellow, IEEE*, Johannes Fischer¹, *Senior Member, IEEE*,
and Lars Zimmermann, *Senior Member, IEEE*

Abstract—Silicon photonic two-dimensional grating couplers for C- and O-band dual-polarization coherent transceivers are analyzed with respect to their polarization splitting/combining performance. Due to scattered light in the grating's plane, a linear cross-polarization results. The latter is responsible for a limited polarization split ratio and a polarizations' non-orthogonality. The impact of these two quantities is evaluated by system-level simulations with regard to OSNR penalties in coherent systems. For both C- and O-band, a design modification for reduced penalties is proposed.

Index Terms—2D grating couplers, polarization splitting, orthogonality, polarization crosstalk, coherent transceivers, silicon photonics.

I. INTRODUCTION

THE continuous traffic growth in the inter- and intra-data center domain has established two major competitors, working towards cost-effective and power-efficient solutions for the upcoming standards. On the one hand, further scaling of the traditional intensity modulated direct detection (IM-DD) schemes is pursued. Alternatively, the adoption of spectrally efficient coherent formats has been proposed, which may be advantageous for data rates beyond 1.6 Tb/s [1]. To make coherent technology attractive for data center interconnects (DCIs), there is still the necessity for further optimization of cost and power consumption.

Manuscript received 15 July 2022; revised 1 September 2022; accepted 10 September 2022. Date of publication 14 September 2022; date of current version 23 September 2022. This work was supported by German Research Foundation and the Open Access Publication Fund of TUBerlin. (*Corresponding author: Galina Georgieva.*)

Galina Georgieva and Klaus Petermann are with the Department of Hochfrequenztechnik-Photonik, Technische Universität Berlin, 10587 Berlin, Germany (e-mail: galina.georgieva@tu-berlin.de; petermann@tu-berlin.de).

Matheus Sena was with the Department of Digital Signal Processing, Fraunhofer Heinrich Herz Institut, 10587 Berlin, Germany. He is now with the Deutsche Telekom AG, 10117 Berlin, Germany (e-mail: matheus.ribeiro-sena@telekom.de).

Johannes Fischer is with the Department of Digital Signal Processing, Fraunhofer Heinrich Herz Institut, 10587 Berlin, Germany (e-mail: johannes.fischer@hhi.fraunhofer.de).

Pascal M. Seiler and Lars Zimmermann are with the Department of Siliziumphotonik, Technische Universität Berlin, 10587 Berlin, Germany, and also with the IHP - Leibniz-Institut für innovative Mikroelektronik, 15236 Frankfurt (Oder), Germany (e-mail: seiler@tu-berlin.de; lars.zimmermann@tu-berlin.de).

Digital Object Identifier 10.1109/JPHOT.2022.3206619

On the way towards cost-optimized communication systems, the silicon photonics (SiP) technology has emerged. The possibility for a monolithic co-integration of photonics and electronics, the utilization of mature (Bi)CMOS foundry processes and the potential for high scalability belong to its most distinctive advantages [2]. Commercial SiP integrated devices for coherent communications are already available, e.g. [3], [4], [5], [6], [7]. Latest experiments, demonstrating a high-performance coherent transmission based on SiP have been reported in [8], [9]. On the other hand, SiP is a high index contrast technology, which is related to a challenging optical coupling and polarization handling. Classical silicon photonic coherent solutions for long-distance communications rely on horizontal couplers, offering a low insertion loss and a high bandwidth [2]. However, in the cost-sensitive DCI domain horizontal couplers may not be sufficiently competitive due to fabrication complexity and lower packaging flexibility. In addition, horizontal couplers tend to require overall a larger chip area due to on-chip fiber alignment structures such as V-grooves. With the DCI economic constraints in mind, two-dimensional grating couplers (2D GCs) are deserving anew attention as a coupling and polarization beam splitting/combining (PBS/C) interface for dual-polarization (DP) coherent transceivers. Although the latter suffer from higher insertion loss and a limited bandwidth, they have two decisive advantages. First, the relaxed packaging tolerances of 2D GCs promise for a reduced packaging cost, which is the most determining factor for the total device expenses [2]. In addition, 2D GCs are presently the most advanced option for wafer-level testing, essential for high-volume manufacturing platforms [2], [10], [11].

With respect to coupling efficiency and polarization-dependent loss (PDL), 2D GCs have been widely studied in the past, e.g. [12], [13], [14], [15], [16], [17], [18], [19], [20], [21] (in chronological order). In our previous publications, we focused on a further aspect, which has been rarely addressed, namely, the polarization spitting behavior of 2D GCs, intended as a PBS/C in DP coherent transmitters and receivers. We have shown that in general 2D GCs convert a part of the power of a given input polarization into its orthogonal counterpart - an effect, which we assign as a linear cross-polarization [22]. We have further indicated in-plane scattering as the physical origin of this conversion [23] - an issue, which inevitably occurs due to

the finite size of the diffracting elements of 2D GCs with respect to the optical waveguide mode. In our most recent work [24], the impact of the cross-polarization has been investigated on system level. We have shown that the cross-polarization is related to a polarization crosstalk, and while at the 2D GC's design central wavelength the polarizations remain orthogonal to each other, at other wavelengths the polarizations' orthogonality is lost. Here, we extend the work from [24] in several aspects. First, we provide a more comprehensive study on polarization related parameters of 2D GCs, namely, the polarization split ratio and the polarizations' angular relation. The latter is furthermore translated to a non-orthogonality PDL, which could result, if the digital signal processing (DSP) algorithm did not take polarizations' non-orthogonality into account. To exclude the last issue, we consider a coherent system with a dedicated DSP algorithm that is able to handle non-orthogonal signals. Using this system model, we analyze the impact of the limited split ratio alone, and in combination with a polarizations' non-orthogonality. For our investigation, designs for conventional C- and O-band 2D GCs are considered first, which comprise a uniform array of circular diffracting elements. Penalties with respect to the optical signal-to-noise ratio (OSNR) are determined, starting with a DP 16 QAM (QAM: quadrature amplitude modulation) as a modulation format. In the second part, design modifications of the 2D GCs are proposed, which could reduce the OSNR penalties, allowing for the enhancement of the usable optical bandwidth. Recently, methods to optimize self-homodyne coherent systems' DSP with regard to a polarization crosstalk was reported in [25]. By contrast, the main objective of the present work is not the DSP development, but the desire to find an optimization method on a device-level, which could minimize sufficiently the polarization crosstalk.

The paper is structured as follows. In Section II, we describe in more detail the methods for the numerical and system-level analysis of different 2D GC designs. In addition, the interplay between the polarizations' split ratio and the polarizations' angular relation is illustrated, indicating our basic expectations for the system's behavior. In Section III conventional 2D GCs are first considered and their relevant parameters are evaluated numerically and transferred to the system model. To reduce the determined penalties and thus make the 2D GCs applicable in a wider optical bandwidth, modified 2D GCs are proposed in the next step. Both numerical and system simulations predict a substantial improvement in all considered aspects. The final conclusions are summarized in Section IV.

II. SIMULATION OF POLARIZATION CROSSTALK

In general, the simulation of the 2D GC's polarization crosstalk goes through two steps:

- i) Numerical device-level simulation: a 2D GC model is prepared in the commercial software by Simulia CST, using the finite-integration-technique (FIT) in time domain [26]. An exemplary model is shown in Fig. 1(a). Each of the two GC arms is excited separately by the

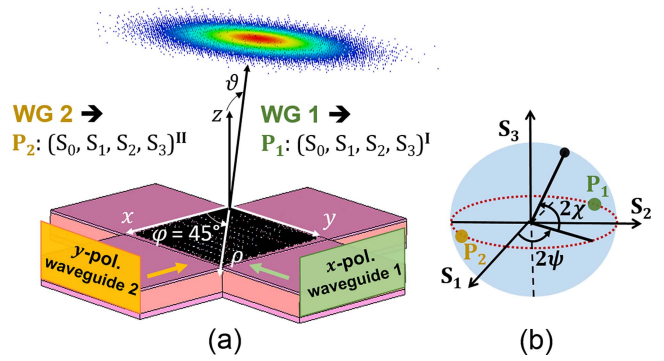


Fig. 1. Determination of the state of polarization of 2D GC's fields: (a) waveguides (WG) 1 and 2 are excited separately, delivering a certain field distribution at a tilted plane with ($\varphi = 45^\circ, \vartheta$). Out of each field distribution, a set of Stokes parameters, related to a polarization state \mathbf{P}_1 or \mathbf{P}_2 results. (b) Out of the angular relation on the Poincaré sphere, the orthogonality relation between the signals from WG 1 and WG 2 can be evaluated.

fundamental transverse-electric TE_{00} mode. In this example, the mode in waveguide (WG) 1 is x -polarized and in WG 2 - y -polarized. After the excitation of WG 1 for instance, the power coupled to a single-mode fiber (SMF) with a preserved x -polarization state is called a target-polarization. The power, converted to its undesired orthogonally polarized counterpart (y -polarization) is assigned as a cross-polarization. The power ratio of the target-to-cross-polarizations (in WG 1 x -to- y) is called a polarization split ratio SR . For an excitation from WG 2, the target- and cross-polarization and the split ratio are defined in opposite. Due to symmetry, the SR from WG 1 and 2 is the same. The polarization split ratio SR is one of the parameters, relevant for the coherent system performance. For a complete physical modeling, the polarization angular relationships between WG 1 and WG 2 has to be determined in addition. Its calculation is shown in more detail in Section II A.

- ii) System-level simulation: the parameters, obtained in i) are substituted in a coherent system simulation model. The latter is described in more detail in Section II B.

A. Methods for the Estimation of Polarization Angles and Non-Orthogonality PDL

In this subsection, our method for the estimation of the orthogonality relation between two polarizations is described in more detail. Out of the derived relation between two polarizations, a corresponding non-orthogonality PDL is determined, which could be present, when the non-orthogonality is not taken into account at the receiver. The latter parameter is used as a figure-of-merit for the evaluation of the non-orthogonality's impact. In the whole analysis, the 2D GCs are considered at the transmitter-side, acting as polarization combiners. Naturally, the same effects are present at the receiver as well. For clarity, we keep our analysis limited to only a single 2D GC at the transmitter with an idealized receiver. The device and system simulations still allow for the demonstration of general dependences, the determination of acceptable performance merits

and the comparison between different 2D GCs designs, used under the same conditions. The polarization analysis is based on results from numerical simulations and is illustrated in Fig. 1(a), where the 2D GC is placed in the Cartesian (x, y, z) -plane. The input transverse-electric TE_{00} fields from WG 1 or 2 are radiated towards a tilted plane, which is rotated by $(\varphi = 45^\circ, \vartheta)$ with respect to the grating's coordinates and corresponds to the position where a SMF would be placed. The angles $(\varphi = 45^\circ, \vartheta)$ for a given target wavelength result from the combination of two 2D GC's design parameters: a non-zero waveguide-to-grating shear angle α [17], [18], [21], [27], [28], [29] and a grating period Λ . In our previous work [30], we derived a system of equations, giving the relationship between the coupling angles (φ, ϑ) and the grating parameters (α, Λ) . To estimate the polarization state of a given out-coupled field, originating from any 2D GC arms, we perform the following procedure. First, WG 1 is excited with the fundamental transverse-electric mode of a silicon waveguide. The radiated field evaluated at the tilted reference plane delivers a set of Stokes parameters $(S_0, S_1, S_2, S_3)^T$ and angles $(2\psi_1, 2\chi_1)$ on the Poincaré sphere (Fig. 1(b)), corresponding to a polarization state \mathbf{P}_1 . The bold font used here denotes a Stokes vector. Next, the procedure is repeated after the excitation of WG 2, resulting in a polarization \mathbf{P}_2 . Exemplary polarization states \mathbf{P}_1 and \mathbf{P}_2 are marked in Fig. 1(b). Out of the angular relation between the angles $(2\psi_1, 2\chi_1)$ and $(2\psi_2, 2\chi_2)$ we are able to determine, whether the two signals are orthogonal or not. The orthogonality condition is:

$$|\psi_2 - \psi_1| = \Delta\psi = 90^\circ$$

$$\chi_1 = -\chi_2.$$

The calculation of the Stokes parameters is based on the procedure used for their practical measurement [31].

$$S_0 = I(0^\circ) + I(90^\circ)$$

$$S_1 = I(0^\circ) - I(90^\circ)$$

$$S_2 = I(45^\circ) - I(135^\circ)$$

$$S_3 = I_{RHC} - I_{LHC},$$

where I is the field intensity of the polarization states, given in the parentheses. The latter are linear $(0^\circ, 90^\circ, 45^\circ, 135^\circ)$ and right-handed or left-handed circular (RHC, LHC). In our case, the intensity is calculated as the square of the magnitude of a given electric field distribution, integrated over the evaluation plane. Since the fields are normalized, the parameter S_0 , giving the total field intensity, is equal to 1. A Stokes vector can be represented in such a case as a set of (S_1, S_2, S_3) . The transformation through polarization plates is described mathematically with the help of their Jones matrices, see e.g. [32]. The degree of polarization (DoP) p and the angles on the Poincaré sphere can be calculated from the Stokes parameters as given in [33]:

$$p = \frac{\sqrt{S_1^2 + S_2^2 + S_3^2}}{S_0}$$

$$S_1 = p \cos 2\chi \cos 2\psi$$

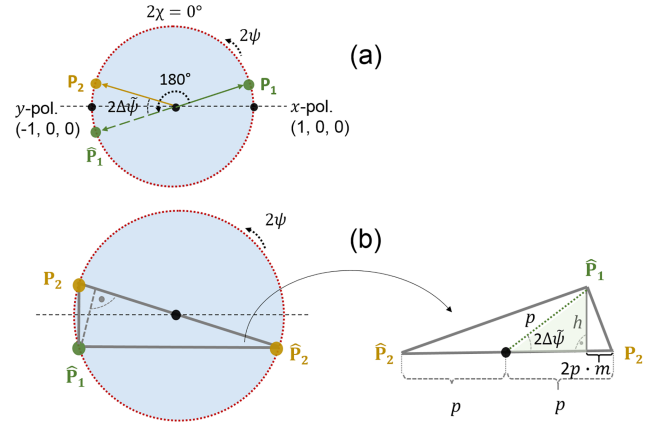


Fig. 2. Exemplary representation of two non-orthogonal polarization states on the Poincaré sphere (in a 2D cross-section). (a) A rotation of the Stokes vector \mathbf{P}_1 by 180° should result in \mathbf{P}_2 . In the non-orthogonal case, the polarization states $\hat{\mathbf{P}}_1, \mathbf{P}_2$ differ by the angle $2\Delta\psi$. (b) A Thales triangle for the determination of a non-orthogonality polarization-dependent loss (PDL).

$$S_2 = p \cos 2\chi \sin 2\psi$$

$$S_3 = p \sin 2\chi$$

$$\Rightarrow 2\psi = \arctan \frac{S_2}{S_1}, \quad 2\chi = \arcsin \frac{S_3}{p}.$$

In a SMF, we obtain a DoP $p = 1$. The presented method delivers an angular difference between two polarizations. A small drawback of this representation is that it does not give a good impression, whether the deviation from the perfect orthogonality is related to a strong penalty or not. In the following, we present a method for the estimation of a PDL, which could result, in case that the polarization de-multiplexing DSP algorithm at the receiver does not take the non-orthogonality into account. We assign the quantity as a non-orthogonality PDL to make it distinguishable from PDL with other physical background. Dedicated DSP algorithms would be necessary to avoid the presence of a non-orthogonality PDL. We explain our calculation procedure for the PDL by setting $2\chi = 0$. In Fig. 2(a), a 2D cross-section of the Poincaré sphere is shown. Here, the exemplary polarization vectors \mathbf{P}_1 and \mathbf{P}_2 are chosen such, that the angular difference is $\Delta 2\psi < 180^\circ$. The DoP of both polarizations is $p = 1$. For orientation, the Stokes vectors of a x -polarization $(1, 0, 0)$ and a y -polarization $(-1, 0, 0)$ are given. For a system with two orthogonal Stokes vectors, we should be able to cancel one of the two polarizations by rotating it by 180° . If the assumption of orthogonality is wrong, an error occurs. To determine this error, we rotate e.g. the Stokes vector \mathbf{P}_1 by 180° , obtaining $\hat{\mathbf{P}}_1$. The polarization states $\hat{\mathbf{P}}_1$ and \mathbf{P}_2 are not identical and differ by the angle:

$$2\Delta\tilde{\psi} = 180^\circ - (2\psi_2 - 2\psi_1) = 180^\circ - 2\Delta\psi. \quad (1)$$

Now, we consider the Thales right-angled triangle in gray, spanned by the end points of $\hat{\mathbf{P}}_1, \mathbf{P}_2, \hat{\mathbf{P}}_2$, where $\hat{\mathbf{P}}_2$ is the orthogonal counterpart of \mathbf{P}_2 (Fig. 2(b)). In the case of orthogonality, the polarizations $\hat{\mathbf{P}}_1$ and \mathbf{P}_2 would be coincident and the depicted triangle would not exist. The latter indicates otherwise different paths between the points $\mathbf{P}_2, \hat{\mathbf{P}}_2$ and $\hat{\mathbf{P}}_1, \hat{\mathbf{P}}_2$.

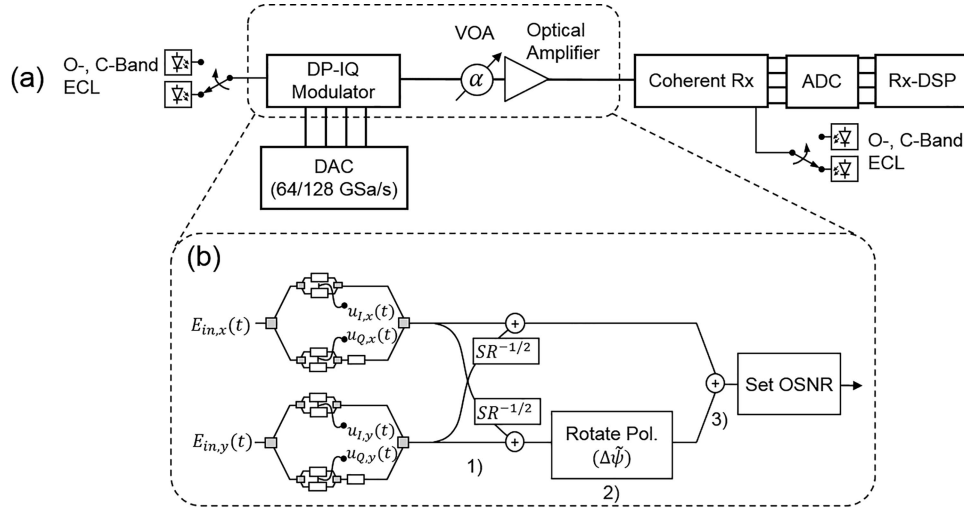


Fig. 3. (a) A coherent transmission setup used in the simulative analysis to evaluate the performance of the optical transmitter based on a 2D grating coupler (2D GC). (b) A model of the set optical modulator + noise-loading station. A polarization crosstalk, determined by the power split ratio SR of two polarizations, is described by the outgoing branches from the output of the IQ modulators (step 1)). A polarization rotation ($\Delta\tilde{\psi}$) is applied in the y -polarization branch (step 2)). The angle $\Delta\tilde{\psi}$ gives a deviation from 90° and is related to a non-orthogonality polarization-dependent loss (PDL). The final addition determines the total polarization crosstalk (step 3)). (Notations: ECL: external cavity laser, DP: dual-polarization, IQ: in-phase quadrature, DAC: digital-to-analog converter, VOA: variable optical attenuator, Rx: receiver, ADC: analog-to-digital converter, DSP: digital signal processing, SR : split ratio, OSNR: optical signal-to-noise ratio).

To account for this deviation, the line segment $2p \cdot m$ can be used, where m is a fraction of the total line length $2p$ between the points \mathbf{P}_2 and $\hat{\mathbf{P}}_2$. With other words, m is defined in the interval $m \in [0, 1]$, its value represents the non-orthogonality PDL. To calculate m as a function of the polarization angles' difference $\Delta\psi$, we apply the geometric mean theorem for the hypotenuse h :

$$h^2 = [p + p(1 - 2m)] \cdot 2pm. \quad (2)$$

Out of the smaller highlighted triangle, we obtain:

$$h = p \sin(2\Delta\tilde{\psi}) \Rightarrow h^2 = p^2 \sin^2(2\Delta\tilde{\psi}). \quad (3)$$

By setting the (2) and (3) to be equal, a quadratic equation for m results in the end. With the boundary condition that m should vanish in the orthogonal case $\Delta\psi = 90^\circ$, i.e. $\Delta\tilde{\psi} = 0^\circ$, the final solution is:

$$\text{PDL} \equiv m = \frac{1}{2} \left(1 - \cos(2\Delta\tilde{\psi}) \right) = \sin^2(\Delta\tilde{\psi}). \quad (4)$$

B. Methods for System Level Simulation and Compensation of Polarization Crosstalk

In the design of optical transceivers, it is crucial that optical sub-components meet specific performance criteria. Particularly for silicon photonic 2D GCs, the impact of polarization crosstalk over different wavelengths in C- and O-band can lead to a non-uniform transmitter system-level performance. The application of powerful DSP-based equalization algorithms plays typically a major role in relaxing device specifications, thus reducing the cost-per-bit of transceiver deployment.

In order to evaluate the performance of silicon photonic 2D GCs as a part of a coherent system, we quantify the OSNR penalty as a relevant figure-of-merit [34]. In essence, the OSNR

penalty is specified by the ratio of the OSNR that is actually required to achieve a certain reference bit-error ratio (BER) and the OSNR that would be theoretically required in an additive white Gaussian noise (AWGN) channel.

In the simulative analysis carried out in this work, we consider the coherent transmission setup depicted in Fig. 3(a), which is simulated using *VPIToolkit DSP Library*. To verify the impact of polarization-combining 2D GCs, the considered DP in-phase quadrature (IQ) modulator is modeled according to the diagram illustrated in Fig. 3(b). In this diagram, the continuous waveform (CW) optical fields in the x - and y -polarization, i.e., $E_{in,x}(t)$ and $E_{in,y}(t)$, are fed to the x - and y -polarization IQ modulators, respectively. Each IQ modulator, in turn, is driven by two electrical signals corresponding to the I and Q quadratures, namely, $u_I(t)$ and $u_Q(t)$. All four quadratures ($u_{I,x}(t)$, $u_{Q,x}(t)$, $u_{I,y}(t)$, $u_{Q,y}(t)$) are generated with 32/64-GBd pseudo-random bit stream sequences from a multi-channel digital-to-analog converter (DAC) (sampling rate of 64/128 GSa/s) with a pattern length of $2^{15}-1$ and a root-raised cosine (RRC) pulse shaping with a roll-off factor of 0.1. Two modulation formats are applied - DP 16/64 QAM. After the modulation of each CW signal, i.e., $E_{in,x}(t)$ and $E_{in,y}(t)$, polarization crosstalk is modeled by the two outgoing branches from the outputs of the IQ modulators (step 1)). This mutual "leakage" from one polarization to another is scaled by $SR^{-1/2}$, as the split ratio SR embodies the power ratio between the x and y tributaries. Subsequently, a polarization rotation, denoted by $\Delta\tilde{\psi}$, is applied on the resulting signal in the y -polarization (step 2)) before the x and y signals are finally combined (step 3)). The angle $\Delta\tilde{\psi}$ gives a deviation from 90° , i.e. $\Delta\tilde{\psi} = 90^\circ - \Delta\psi$, as given in (1). In addition, $\Delta\tilde{\psi}$ is directly related to a non-orthogonality PDL, as can be seen in (4). To perform the wavelength sweep in the O- (1290–1330 nm) and C-band (1520–1560 nm), external cavity lasers (ECL)s on the

transmitting side as well as on the receiving side (local oscillator (LO)) are added with some constant relaxation assumptions: linewidth (100 kHz), power level (0 dBm). Modulators are also simplified in terms of constant $V_\pi = 1$ V. Since this analysis solely concerns the back-to-back performance of the transmitter, a noise loading station, composed of a variable optical attenuator (VOA) and an optical amplifier, is inserted between transmitter and receiver in order to enable a sweep of OSNR values. This function is abstracted in the model by the ‘‘Set OSNR’’ block, which simply varies the amount of AWGN in the signal in order to obtain different BER measurements.

At the coherent receiver (Rx), the only considered impairment originates from the LO frequency offset (1 GHz). Other than that, the coherent Rx is assumed ideal for the considered wavelength interval as we focus on the penalties originating on the transmitter side. After signal reception, the four quadratures are digitized at 64/128 GSa/s by an analog-to-digital converter (ADC) and finally forwarded to the Rx-DSP chain. The first functional block of the Rx-DSP is a matched filter to remove the contribution of the pulse shaping. Following that, the signal tributaries are delivered to a frequency-domain data-aided adaptive equalizer [35]. This algorithm requires that three header sequences (binary phase-shift keying (BPSK) and quaternary PSK (QPSK) symbols) be inserted at the transmitter DSP, which can be used for frame synchronization, carrier frequency offset (CFO) compensation and channel estimation at the receiver DSP. In the channel estimation, constant-amplitude-zero autocorrelation (CAZAC) sequences [36], consisting of 16 QPSK symbols, are primarily used to update a 2×2 multi-input multi-output (MIMO) frequency-domain equalizer for polarization separation and for channel impairments compensation. Based on the estimated channel transfer function, the equalizer coefficients are computed with a minimum mean square error (MMSE) constraint [36]. At last, a carrier phase compensation based on blind phase search [37] is carried out before symbol decision for BER measurement.

C. Interplay Between Split Ratio and Non-Orthogonality

Before analyzing particular 2D GC designs, the interdependence of the polarizations’ split ratio and non-orthogonality will be illustrated here. This will support the result’s interpretation at a later stage. Considering again the adapted modulator model in Fig. 3(b), the interaction between the x - and y -branch after IQ modulation is divided into three steps:

- 1) Superposition due to a finite split ratio SR .
- 2) Orthogonality deterioration, an additional crosstalk term results. The latter may be applied to only one or both branches, which makes no difference after the receiver DSP. For simplicity, a rotation at the y -branch only is chosen with $\Delta\tilde{\psi} = 90^\circ - \Delta\psi$. The order, in which split ratio and polarization rotation are implemented, can be inverted.
- 3) Addition of the new crosstalk term, resulting from the polarization rotation.

The intermediate steps can be written in the following way, whereat only the signals’ amplitudes are given and in-phase relation between both polarizations is assumed.

- 1) Superposition, assuming equal x -to- y and y -to- x power split ratio SR :

$$\begin{aligned}\hat{E}_x &= \left(1 - \frac{1}{\sqrt{SR}}\right)E_x + \frac{1}{\sqrt{SR}}E_y \\ \hat{E}_y &= \left(1 - \frac{1}{\sqrt{SR}}\right)E_y + \frac{1}{\sqrt{SR}}E_x.\end{aligned}$$

- 2) Rotation of \hat{E}_y by $\Delta\tilde{\psi}$:

$$\begin{aligned}M_y &= \begin{bmatrix} \cos(\Delta\tilde{\psi}) & -\sin(\Delta\tilde{\psi}) \\ \sin(\Delta\tilde{\psi}) & \cos(\Delta\tilde{\psi}) \end{bmatrix} \\ M_y \cdot \begin{bmatrix} 0 \\ \hat{E}_y \end{bmatrix} &= \begin{bmatrix} -\sin(\Delta\tilde{\psi}) \\ \cos(\Delta\tilde{\psi}) \end{bmatrix} \cdot \hat{E}_y.\end{aligned}$$

- 3) Addition of the extra x -term to \hat{E}_x :

$$\begin{aligned}\hat{\hat{E}}_x &= \hat{E}_x - \sin(\Delta\tilde{\psi})\hat{E}_y \\ \hat{\hat{E}}_y &= \cos(\Delta\tilde{\psi})\hat{E}_y.\end{aligned}$$

Since \hat{E}_y contains partially the initial E_x signal, in the x -branch some of the original bit sequence can be ‘‘re-gained’’ for an appropriate $\Delta\tilde{\psi} \neq 0$. In the same time, more crosstalk from E_y will be added. Particularly, we obtain for the x -polarization:

$$\begin{aligned}\hat{\hat{E}}_x &= \left[1 - \frac{1}{\sqrt{SR}} - \sin(\Delta\tilde{\psi})\frac{1}{\sqrt{SR}}\right]E_x \\ &+ \left[\frac{1}{\sqrt{SR}} - \sin(\Delta\tilde{\psi})\left(1 - \frac{1}{\sqrt{SR}}\right)\right]E_y.\end{aligned}\quad (5)$$

For $\Delta\tilde{\psi} < 0$, that is $\Delta\psi > 90^\circ$, the original signal amplitude E_x is partially recovered, but more crosstalk E_y is added as well. Interestingly, for $\Delta\tilde{\psi} > 0$ or $\Delta\psi < 90^\circ$, a part of the initially added E_y (step 1)) is subtracted and the crosstalk is reduced. This means that the corresponding penalty will be reduced. However, the original signal amplitude E_x decreases as well, so that the apparent advantage of a non-orthogonality with $\Delta\psi < 90^\circ$ has its price in the end.

To illustrate this behavior, an exemplary simulation is performed without a DSP activation. A QPSK transmission is considered and the constellations of the x -polarization are shown for three cases with a constant split ratio SR , namely: 1) $SR = 12$ dB, $\Delta\tilde{\psi} = 0^\circ$, $\Delta\psi = 90^\circ$ (orthogonal case), 2) $SR = 12$ dB, $\Delta\tilde{\psi} = -12^\circ$, $\Delta\psi = 102^\circ$, 3) $SR = 12$ dB, $\Delta\tilde{\psi} = 12^\circ$, $\Delta\psi = 78^\circ$ (Fig. 4). The values of interest are the signal amplitude (distance from the origin of the IQ diagram to the constellation point) and the error vector magnitude (EVM). In this example, the EVM and the amplitude of the y -constellation change only little, because the y -signal is only scaled by the factor $\cos(\Delta\tilde{\psi})$, which is in all cases nearly 1. For that reason, the y -constellation is not shown,

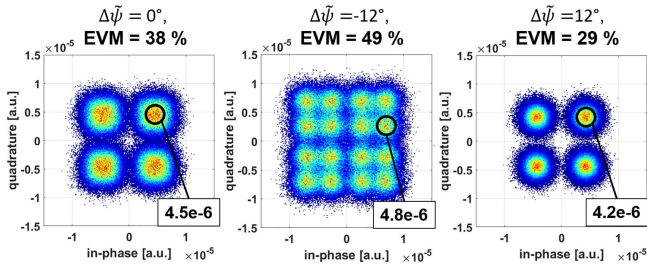


Fig. 4. Constellations of the x -polarization of a QPSK signal, for which a fixed polarizations' split ratio is assumed. The orthogonality deviation $\Delta\psi$ is varied to account for different polarization crosstalk levels. $\Delta\psi = 0^\circ$, ($\Delta\psi = 90^\circ$, orthogonal case), $\Delta\psi = -12^\circ$ ($\Delta\psi = 102^\circ$), $\Delta\psi = 12^\circ$ ($\Delta\psi = 78^\circ$).

being the same as the x -constellation in the orthogonal case. The behavior described above by (5) can be clearly seen, when we look at the three x -constellations. In the first case of orthogonal signals the EVM is 38% with a signal magnitude of $4.5 \cdot 10^{-6}$ (in arbitrary units). The EVM becomes worse (49%) in the case of an orthogonality deviation with $\Delta\psi > 90^\circ$ - the constellation looks rather like a 16 QAM (a similar effect has been shown in [38] for an in-band crosstalk). In opposite, the EVM improves to 29% in the case of $\Delta\psi < 90^\circ$. In the same time, the signal's amplitude drops from $4.7 \cdot 10^{-6}$ ($\Delta\psi > 90^\circ$) to $4.2 \cdot 10^{-6}$ ($\Delta\psi < 90^\circ$). The signal amplitude's change is also an indication for the non-orthogonality PDL, whereat the different scenarios show the cases, when the amplitude of the x -signal becomes larger or smaller than the amplitude of the y -signal. The exemplary values given here are determined by the chosen split ratio. Note that this example does not represent ideally the case of a 2D GC, because the latter has a different split ratio for any $\Delta\psi$, resp. $\Delta\psi$.

III. EVALUATION OF 2D GRATING COUPLERS FOR C- AND O-BAND

Using the methods given in the previous section, we compare here exemplary 2D GCs for C- and O-Band within a 40 nm bandwidth around their central wavelengths both numerically and in coherent system simulations. O-band coherent systems are also discussed as a potential candidate for next generation DCIs [39]. All C- and O-band 2D GCs are specifically designed under the boundary conditions of the photonic BiCMOS platform that we use [40], [41]. Material and geometric specifics as well as the restrictions of the 248 nm DUV lithography that we use are taken into account. We consider standard silicon rib waveguides with a 220 nm silicon on 2 μm silicon dioxide. The rib slab is defined with the same etch depth as the grating. All 2D GCs have a coupling angle $\vartheta = 8^\circ$ at the symmetry plane. Below, we begin with conventional designs, as those used in our previous work [24].

A. Uniform 2D Grating Couplers

The first 2D GC designs studied here comprise a uniform array of circular diffracting elements. The following geometries are used for C- and O-band respectively:

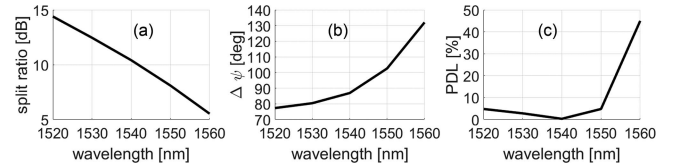


Fig. 5. Simulated parameters of a C-band 2D GC, comprising a uniform array of circular diffracting elements. (a) Polarizations' split ratio, (b) polarizations' angular difference $\Delta\psi$ and (c) the corresponding non-orthogonality polarization-dependent loss (PDL).

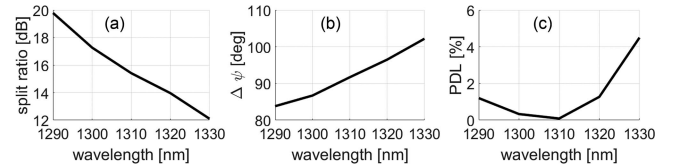


Fig. 6. Simulated parameters of an O-band 2D GC, comprising a uniform array of circular diffracting elements. (a) Polarizations' split ratio, (b) polarizations' angular difference $\Delta\psi$ and (c) the corresponding non-orthogonality polarization-dependent loss (PDL).

- *C-band*: a waveguide-grating shear angle $\alpha = 2^\circ$, a grating period $\Lambda = 622$ nm, a diffracting elements' diameter $w_L = 440$ nm, an etch depth $d = 120$ nm.
- *O-band*: a waveguide-grating shear angle $\alpha = 2^\circ$, a grating period $\Lambda = 480$ nm, a diffracting elements' diameter $w_L = 280$ nm, an etch depth $d = 120$ nm.

The numerical results are obtained by the Simulia's CST FIT time-domain solver. The simulations consider transmitter-side out-coupling 2D GCs, when either of their two waveguide arms is excited. Power coupling spectra are shown in Appendix A. The maximal coupling efficiency in C- and O-band is -5 dB at 1540 nm and -3.3 dB at 1310 nm. Thus, we consider the bandwidth 1520–1560 nm for the C-band 2D GC and 1290–1330 nm for the O-band 2D GC. Figs. 5 and 6 show simulated parameters of interest for the C- and O-band 2D GC respectively. In both cases, the split ratio deteriorates with an increasing wavelength. Although the parameter reaches better values in O-band, for both structures levels no better than 20 dB can be achieved. With respect to efficiency and polarization splitting, the O-band 2D GC outperforms its C-band counterpart. The reason is that in efficiency-optimized designs for our technology, the parasitic in-plane scattering in O-band 2D GCs is lower than in C-band ones. In-plane scattering prevents the light being out-coupled from the grating towards the coupling fiber. In addition, the latter effect enhances the cross-polarization. The lower scattering in O-band 2D GCs can be explained by the smaller size of their diffracting elements with respect to the wavelength, which is given by the boundaries of our technology. Fabrication platforms with other characteristics may be more suitable for C-band designs. The remaining two coupled parameters - the polarization angles' difference $\Delta\psi$ and the corresponding non-orthogonality PDL depend rather on the phase of the radiated parasitic in-plane scattered fields. Note that the polarization angles χ_1, χ_2 are not taken into account, because they do not deviate significantly from 0° . The polarizations remain orthogonal at the corresponding

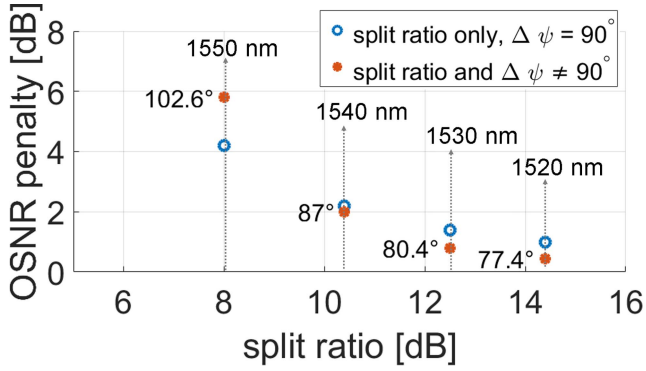


Fig. 7. A uniform 2D GC for C-band: OSNR penalties (at a BER of 10^{-3}), when only a limited split ratio is considered, and when the limited split ratio is combined with a non-orthogonal polarizations' angular relation $\Delta\psi$.

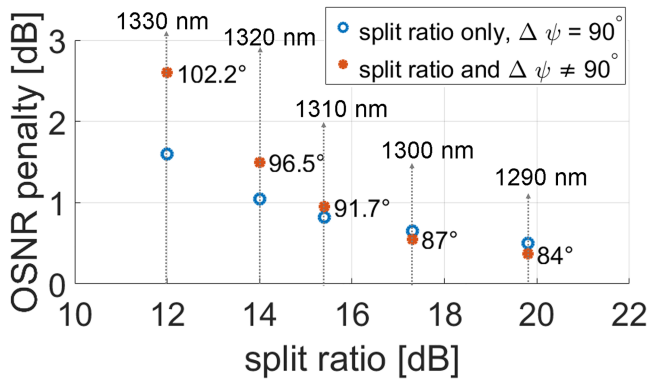


Fig. 8. A uniform 2D GC for O-band: OSNR penalties (at a BER of 10^{-3}), when only a limited split ratio is considered, and when the limited split ratio is combined with a non-orthogonal polarizations' angular relation $\Delta\psi$.

grating's central wavelength (1540 nm and 1310 nm resp.) and deviate from the orthogonality state otherwise. It is noticeable that the orthogonality deviation is more distinctive in C-band, leading to a strong non-uniformity of $\Delta\psi$ (from 77° to 132°). The corresponding PDL may reach up to 45%. By contrast, the PDL remains below 5% in O-band (with a $\Delta\psi$ range from 84° to 102°). While the PDL values will not be visible in a system with an appropriate DSP, their levels are a measure for the performance quality of each structure. Next, using the split ratio and $\Delta\psi$ values from Figs. 5(a), (b) and 6(a), (b), the performance of both 2D GCs as a part of a DP 16 QAM coherent system is evaluated. An exemplary symbol rate of 32 GBd is chosen for that purpose. The OSNR penalty is determined at a BER of 10^{-3} with an uncertainty of about 0.1 dB. Because the DSP eliminates the differences between both polarizations, the results for only one of them are shown. Two scenarios are considered: 1) split ratio only, which means that a given split ratio is implemented under the assumption of orthogonality 2) split ratio and $\Delta\psi \neq 90^\circ$ - the exact split ratio- $\Delta\psi$ combinations from Figs. 5(a), (b) and 6(a), (b) are used. Figs. 7 and 8 show the simulated OSNR penalty (at a BER of 10^{-3}) vs. split ratio for the two cases in C- and O-band respectively. For each combination

of split ratio and $\Delta\psi$, the corresponding wavelength is marked. Note that the given $\Delta\psi$ values are related to the pre-DSP non-orthogonality PDL, according to (1), (4). The expectations from the numerical analysis are directly translated into the system-level simulations. Apparently, the resulting penalties in C-band are significantly larger. For the most extreme case at a 1560 nm wavelength, in which both the split ratio and the orthogonality are strongly deteriorated, the target OSNR level is not reached. For that reason, the point is missing in Fig. 7. Noticeably, an OSNR penalty results also in the orthogonality cases, in which only a finite split ratio is present. The impact of the latter parameter is thus not equivalent to a polarization rotation in the SMF. The OSNR penalty scales with a decreasing split ratio. This indicates that there are limitations for the DSP, which prohibit the perfect separation of both polarizations. The reason is that a maximization of a signal, combined with a perfect crosstalk elimination is not reachable. To support this statement, an exemplary calculation is given in the Appendix B. The most possible explanation for this limitation is the fact that signal and cross-polarization have a different fiber coupling efficiency. Adapted DSP would be required to reduce the impact of the finite split ratio.

After the additional consideration of the polarizations' non-orthogonality, in both C- and O-band we observe the interesting case of an "improvement" of the OSNR penalty for angular differences $\Delta\psi < 90^\circ$. As already explained, this is a result from the small counter-reaction of the non-orthogonality-related crosstalk against the split-ratio-related crosstalk. Since this occurs at wavelengths with a comparatively high split ratio, the apparent benefit is small: 0.4–0.7 dB. Although we use the support of a powerful DSP compensation and neglect additional system impairments, the OSNR penalties within the considered bandwidths are too large. If we permit maximally 1 dB deterioration, the C-band 2D GC may be used only at a single wavelength (1520 nm), which does not correspond to the wavelength of a maximal coupling efficiency. The O-band design may be used in the range 1290–1310 nm, which is not centered around the maximum transmission's wavelength. Moreover, these statements apply to a single 2D GC. The application of 2D GCs at both transmitter and receiver will introduce even larger limitations. The expected bandwidth constraints in [24] are confirmed by the system-level analysis.

B. Segmented 2D Grating Couplers

The results in the previous subsection show that the initial 2D GC designs require a modification to reduce the OSNR penalty in a coherent system and potentially to allow for the utilization of a larger optical bandwidth. Here, a simple design modification is proposed. The idea behind that is the following. Previous analyses state that polarization-related issues can be attributed to a scattering in the grating's plane. The latter is particularly strong, when an array of elements with identical scattering properties is given [23]. This is the case of uniform 2D GCs. To reduce the overall in-plane scattering strength, diffracting elements with different local scattering profiles may be

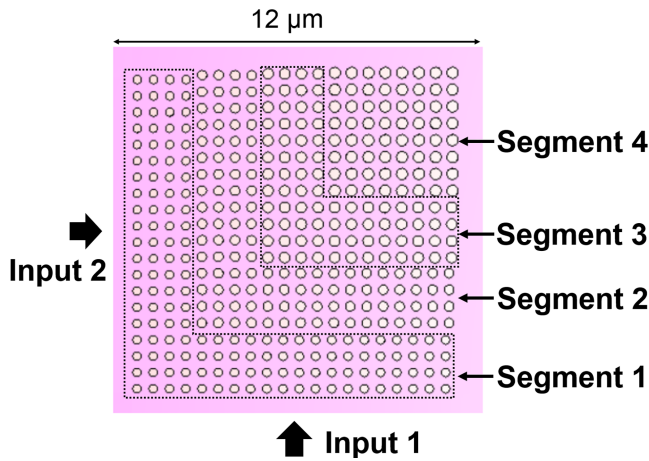


Fig. 9. A segmented 2D grating coupler. In this example, 4 segments are chosen. A segment i comprises circular diffracting elements with the diameter $w_{L,i}$ and the periodicity Λ_i . It is required that $w_{L,1} < w_{L,2} < w_{L,3} < w_{L,4}$ and $\Lambda_1 < \Lambda_2 < \Lambda_3 < \Lambda_4$.

considered. The simplest way to realize that is to choose diffracting elements with different sizes. For a constant diffraction angle, the periodicity must be adapted according to the size difference. To reduce the design complexity, we may limit the number of different sizes and periods and group the diffracting elements into segments, as shown in Fig. 9. The exemplary design in this work comprises 4 segments. A segment i includes circular diffracting elements with the same diameter $w_{L,i}$ and the periodicity Λ_i . The diffracting elements in the first segment $i = 1$ have the smallest dimensions and the shortest periodicity. The elements' size and periodicity increase with increasing number of segments, i.e. $w_{L,1} < w_{L,2} < w_{L,3} < w_{L,4}$ and $\Lambda_1 < \Lambda_2 < \Lambda_3 < \Lambda_4$. For the diameter's difference, an increment of at least 20 nm is preferred, ensuring that the difference will be available after fabrication. The principle of segmented 2D GCs is very similar to the idea of apodization/chirping, but no mode field overlap optimization is pursued. For that reason, a little number of segments may be chosen.

In the following, the geometric specifics of a C- and O-band segmented 2D GC are listed:

- *C-band*: a waveguide-grating shear angle $\alpha = 2^\circ$, grating periods $\Lambda_i = 583/591/599/603$ nm, circular diffracting elements with a local diameter $w_{L,i} = 300/340/380/400$ nm, etch depth $d = 100$ nm.
- *O-band*: a waveguide-grating shear angle $\alpha = 2^\circ$, grating periods $\Lambda_i = 463/471/479/483$ nm, circular diffracting elements with a local diameter $w_{L,i} = 180/220/260/280$ nm, etch depth $d = 100$ nm.

The shallower etch depth for the segmented designs is determined by the smallest diffracting elements' diameter in O-band, which may not go below 180 nm. The perturbation strength in the first segment is reduced by the shallower etch depth.

Now, the numerical simulations from the previous subsection are repeated and the same parameters are extracted. Simulated coupling spectra are shown in the Appendix A as well. A minor change of the coupling efficiency results: -4.8 dB in C-band

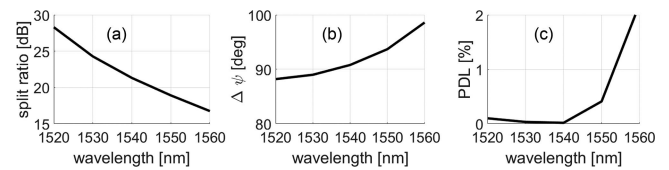


Fig. 10. Simulated parameters of a C-band 2D GC, comprising 4 segments with circular diffracting elements of different size and periodicity. (a) Polarizations' split ratio, (b) polarizations' angular difference $\Delta\psi$ and (c) the corresponding non-orthogonality polarization-dependent loss (PDL).

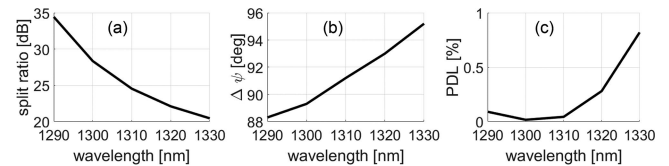


Fig. 11. Simulated parameters of an O-band 2D GC, comprising 4 segments with circular diffracting elements of different size and periodicity. (a) Polarizations' split ratio, (b) polarizations' angular difference $\Delta\psi$ and (c) the corresponding non-orthogonality polarization-dependent loss (PDL).

and -3.6 dB in O-band at the same central wavelengths. A small variation of 0.2–0.3 dB is acceptable, being within the measurement and simulation accuracy limits. The efficiency deviation in this case results due to small changes in the out-coupled power strength. Figs. 10 and 11 show the results in C- and O-band respectively. In both cases, a significant improvement is achieved in all aspects. In C-band, the split ratio is at least 10 dB better within the considered bandwidth. The deviation from the orthogonality state is maximally 8° with a better correction at lower wavelengths. Accordingly, the non-orthogonality PDL is $< 2\%$ within the evaluated bandwidth. The segmentation in O-band allows for the achievement of even better split ratios of > 20 dB. The $\Delta\psi$ range is reduced to the interval from 88° to 96° . The maximal non-orthogonality PDL is lower than 1%. Once again, the O-band 2D GC outperforms its C-band equivalent.

Next, the coherent systems' simulations are carried out, using the parameters from Figs. 10(a), (b) and 11(a), (b). This time, we do not compare the scenarios "split ratio only" and "split ratio and $\Delta\psi \neq 90^\circ$," because the same effects can be observed. Instead of this, different modulation formats and/or symbol rates are considered, namely, the original DP 16 QAM, 32 GBd, extended by DP 16 QAM, 64 GBd and DP 64 QAM, 64 GBd. In all cases, the non-orthogonality is taken into account. Figs. 12 and 13 show the results for the segmented C- and O-band design respectively. Since the 2D GCs' performance has no relation to the symbol rate and no electrical bandwidth limitations are included, we observe, as expected, almost no difference between DP 16 QAM 32 GBd and 64 GBd. Small deviations below 0.1 dB occur due to the uncertainty of the penalty's determination. By contrast, DP 64 QAM is more sensitive with respect to split ratio limitations. The optimal C-band design combined with a suitable polarization non-orthogonality handling DSP scheme ensures no more than 1.5 dB OSNR penalty at a BER of 10^{-3} . The improved O-band design delivers even better performance with an OSNR penalty below 1 dB, allowing for an operation within

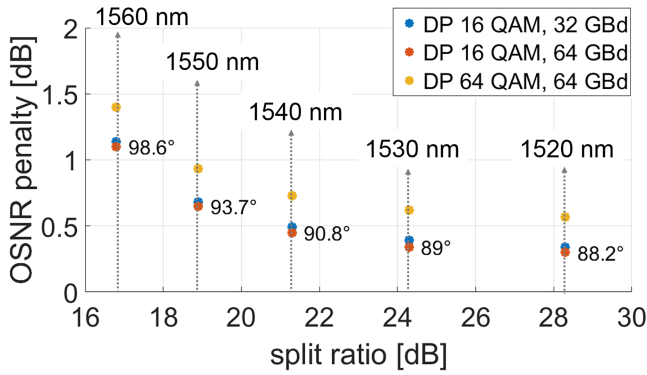


Fig. 12. A segmented 2D GC for C-band: OSNR penalties for different modulation formats and/or symbol rates. Both limited split ratio and polarizations' non-orthogonality are considered.

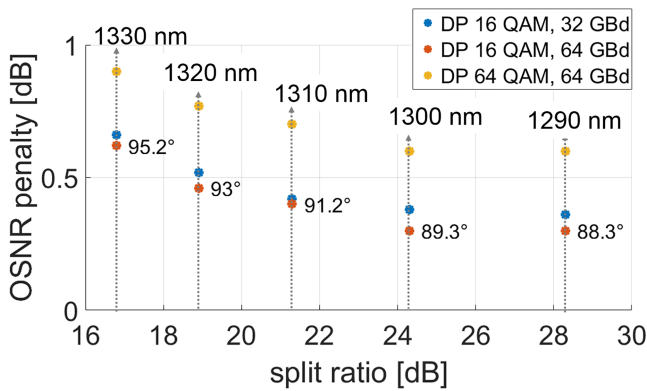


Fig. 13. A segmented 2D GC for O-band: OSNR penalties for different modulation formats and/or symbol rates. Both limited split ratio and polarizations' non-orthogonality are considered.

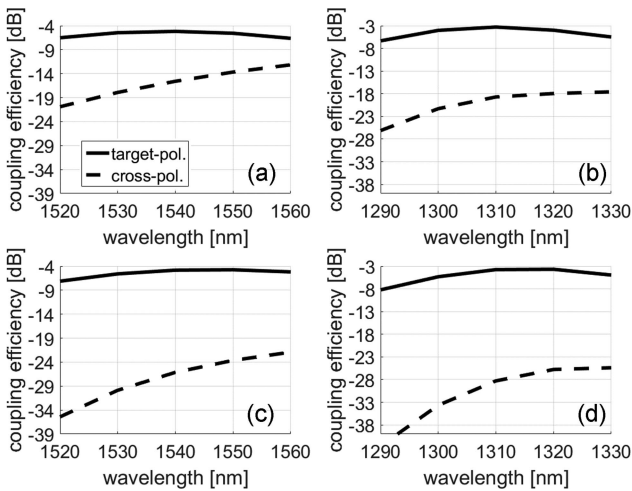


Fig. 14. Coupling efficiency of the target- vs. cross-polarization of (a) a uniform C-band 2D GC, (b) a uniform O-band 2D GC, (c) a segmented C-band 2D GC, (d) a segmented O-band 2D GC.

the full analyzed bandwidth. If we consider a combination of a transmitter- and receiver-side 2D GC, we can basically expect a maximally 3 dB worse total split ratio deterioration and further polarization rotation. With regard to this matter, a design with a larger tolerance against split ratio and non-orthogonality is

preferable. Considering that, the segmented O-band 2D GC shows more advantages compared to its C-band equivalent and its application in DP 16 QAM coherent systems would be reasonable. This adds further arguments to the discussion on O-band coherent DCIs [39].

IV. CONCLUSION

We analyzed the impact of a polarization crosstalk in coherent systems, caused by the physical limitations of silicon photonic 2D GCs. Numerical simulations in C- and O-band were used to extract relevant 2D GC parameters. The interplay between two crosstalk sources - the polarizations' split ratio and the polarizations' angular relation $\Delta\psi$ was shown. For a non-orthogonality $\Delta\psi < 90^\circ$, a small crosstalk cancellation can result. The system-level simulations of non-optimized 2D GCs showed that the OSNR deterioration can be a restricting factor for the usable GC bandwidth. To allow for reduced OSNR penalties and a broadband operation, optimized segmented 2D GCs were proposed. Particularly good results were obtained for the segmented O-band 2D GC, which could be able to keep the OSNR penalty in a transceiver below 1 dB. Our analysis confirmed that O-band 2D GCs designed for our technology have clear advantages over their C-band equivalents. Segmented O-band 2D GCs can be a suitable coupling and polarization splitting/combining interface in DP 16 QAM silicon photonic coherent systems.

APPENDIX A

For completeness, the simulated coupling spectra of the uniform and segmented 2D GCs are shown here. Fig. 14(a) and (b) shows the results for the uniform 2D GCs in C- and O-band. Fig. 14(c) and (d) shows the results for the segmented 2D GCs in C- and O-band. The plots include the desired target- vs. the parasitic cross-polarization (single waveguide excitation). Due to symmetry, the results are the same, regardless of the source waveguide. While in segmented 2D GCs the coupling efficiency of the target-polarization remains almost unchanged, the cross-polarization strength is significantly reduced. This is the key for the improvement of all device performance metrics, which are related to the polarization handling capabilities.

APPENDIX B

The limited DSP capability to separate two polarizations due to the finite 2D GC's split ratio, is illustrated here in a short example. We consider the orthogonal case, in which two signals are given as a superposition of an original polarization x and y with an added crosstalk term, dependent on the split ratio SR (cf. Section II, C).

$$\hat{E}_x = \left(1 - \frac{1}{\sqrt{SR}}\right)E_x + \frac{1}{\sqrt{SR}}E_y$$

$$\hat{E}_y = \left(1 - \frac{1}{\sqrt{SR}}\right)E_y + \frac{1}{\sqrt{SR}}E_x.$$

We look for a rotation matrix M_δ with an appropriate angle δ , which guarantees that the original signal will be maximized and the crosstalk term will vanish (considering \hat{E}_x or \hat{E}_y):

$$M_\delta = \begin{bmatrix} \cos \delta & -\sin \delta \\ \sin \delta & \cos \delta \end{bmatrix}$$

$$M_\delta \cdot \begin{bmatrix} \hat{E}_x \\ \hat{E}_y \end{bmatrix} = \begin{bmatrix} \cos \delta \hat{E}_x - \sin \delta \hat{E}_y \\ \sin \delta \hat{E}_x + \cos \delta \hat{E}_y \end{bmatrix}.$$

Particularly, for the x -polarized signal we obtain:

$$\hat{E}_{x,\delta} = \cos \delta \left(1 - \frac{1}{\sqrt{SR}} \right) E_x + \frac{\cos \delta}{\sqrt{SR}} E_y$$

$$- \sin \delta \left(1 - \frac{1}{\sqrt{SR}} \right) E_y - \frac{\sin \delta}{\sqrt{SR}} E_x.$$

To maximize the original signal and eliminate the crosstalk, the following equations should be fulfilled:

$$\cos \delta \left(1 - \frac{1}{\sqrt{SR}} \right) - \frac{\sin \delta}{\sqrt{SR}} = 1 \quad \text{maximal signal}$$

$$\frac{\cos \delta}{\sqrt{SR}} - \sin \delta \left(1 - \frac{1}{\sqrt{SR}} \right) = 0 \quad \text{crosstalk elimination.}$$

The system of equations has a solution in two cases. The first one is the ideal case of $SR \rightarrow \infty$, in which the 2D GC combines or separates the original polarizations perfectly. The second one is the unusual case of $SR = 1$, which represents a situation, in which both polarizations will completely change their role, that is, x becomes y and y becomes x . In any other scenario, the crosstalk elimination will not correspond to a maximal signal amplitude, which explains the existing OSNR penalty after the presently applied DSP.

REFERENCES

- [1] X. Zhou, R. Urata, and H. Liu, "Beyond 1 tb/s intra-data center interconnect technology: IM-DD or coherent?," *J. Lightw. Technol.*, vol. 38, no. 2, pp. 475–484, 2020, doi: [10.1109/JLT.2019.2956779](https://doi.org/10.1109/JLT.2019.2956779).
- [2] C. Doerr and L. Chen, "Silicon photonics in optical coherent systems," *Proc. IEEE*, vol. 106, no. 12, pp. 2291–2301, Dec. 2018, doi: [10.1109/JPROC.2018.2866391](https://doi.org/10.1109/JPROC.2018.2866391).
- [3] R. Nagarajan, I. Lyubomirsky, and O. Agazzi, "Low power DSP-based transceivers for data center optical fiber communications," *J. Lightw. Technol.*, vol. 39, no. 16, pp. 5221–5231, 2021, doi: [10.1109/JLT.2021.3089901](https://doi.org/10.1109/JLT.2021.3089901).
- [4] Marvell Semiconductor Inc., "Deneb 400 G Multi-rate Coherent DSP, Product Brief," 2021. Accessed: Sep. 17, 2022. [Online]. Available: <https://www.marvell.com/products/coherent-dsp.html>
- [5] J. Zhou, J. Wang, L. Zhu, and Q. Zhang, "Silicon photonics for 100 gbaud," *J. Lightw. Technol.*, vol. 39, no. 4, pp. 857–867, 2021, doi: [10.1109/JLT.2020.3009952](https://doi.org/10.1109/JLT.2020.3009952).
- [6] NeoPhotonics, "White Paper - Photonic IC Enabled Coherent Optical Systems," Accessed: Sep. 17, 2022. [Online]. Available: <https://www.lumentum.com/en/neophotonics-products>
- [7] Acacia Communications, Inc. (now part of Cisco, Inc.), "Acacia unveils industry's first single carrier 1.2 T multi-haul pluggable module," Sep. 23, 2021, Online: <https://acacia-inc.com/blog/acacia-unveils-industrys-first-single-carrier-1-2t-multi-haul-pluggable-module/>
- [8] Z. Zheng et al., "Transmission of 120 gbaud QAM with an all-silicon segmented modulator," *J. Lightw. Technol.*, vol. 40, no. 16, pp. 5457–5466, Aug. 2022, doi: [10.1109/JLT.2022.3180981](https://doi.org/10.1109/JLT.2022.3180981).
- [9] E. Berikaa et al., "Silicon photonic single-segment IQ modulator for net 1 Tbps/λ transmission using all-electronic equalization," *J. Lightw. Technol.*, early access, Jul. 14, 2022, doi: [10.1109/JLT.2022.3191244](https://doi.org/10.1109/JLT.2022.3191244).
- [10] R. Marchetti, C. Lacava, L. Carroll, K. Gradkowski, and P. Minzioni, "Coupling strategies for silicon photonics integrated chips," *Photon. Res.*, vol. 7, no. 2, pp. 201–239, 2019, doi: [10.1364/PRJ.7.000201](https://doi.org/10.1364/PRJ.7.000201).
- [11] T. Pinguet et al., "High-volume manufacturing platform for silicon photonics," *Proc. IEEE*, vol. 106, no. 12, pp. 2281–2290, Dec. 2018, doi: [10.1109/JPROC.2018.2859198](https://doi.org/10.1109/JPROC.2018.2859198).
- [12] F. Boeuf et al., "A multi-wavelength 3D-compatible silicon photonics platform on 300 mm SOI wafers for 25 Gb/s applications," in *Proc. IEEE Int. Electron Devices Meeting*, 2013, pp. 13.3.1–13.3.4, doi: [10.1109/IEDM.2013.6724623](https://doi.org/10.1109/IEDM.2013.6724623).
- [13] L. Verslegers et al., "Design of low-loss polarization splitting grating couplers," in *Proc. Adv. Photon. Commun.*, 2014, Art. no. JT4A.2, doi: [10.1364/IPRSN.2014.JT4A.2](https://doi.org/10.1364/IPRSN.2014.JT4A.2).
- [14] C. Baudot et al., "Low cost 300 mm double-SOI substrate for low insertion loss 1D & 2D grating couplers," in *Proc. 11th Int. Conf. Group IV Photon.*, 2014, pp. 137–138, doi: [10.1109/Group4.2014.6961964](https://doi.org/10.1109/Group4.2014.6961964).
- [15] J. Zou, Y. Yu, and X. Zhang, "Two-dimensional grating coupler with a low polarization dependent loss of covering the C-band," *Opt. Lett.*, vol. 41, no. 18, pp. 4206–4209, 2016, doi: [10.1364/OL.41.004206](https://doi.org/10.1364/OL.41.004206).
- [16] S. Plantier, D. Fowler, K. Hassan, O. Lemonnier, and R. Orobtcouk, "Impact of scattering element shape on polarisation dependent loss in two dimensional grating couplers," in *Proc. IEEE 13th Int. Conf. Group IV Photon.*, 2016, pp. 76–77, doi: [10.1109/Group4.2016.7739057](https://doi.org/10.1109/Group4.2016.7739057).
- [17] Y. Sobu, S.-H. Jeong, Y. Tanaka, and K. Morito, "300-mm ArF-immersion lithography technology based si-wire grating couplers with high coupling efficiency and low crosstalk," in *Proc. 21st OptoElectron. Commun. Conf., Int. Conf. Photon. Switching*, 2016, pp. 1–3.
- [18] Y. Sobu, S.-H. Jeong, and Y. Tanaka, "Si-wire two-dimensional grating coupler with polarization-dependent loss of lower than over a 60-nm-wide spectral range," *Japanese J. Appl. Phys.*, vol. 57, 2018, Art. no. 112501, doi: [10.7567/JJAP.57.112501](https://doi.org/10.7567/JJAP.57.112501).
- [19] Y. Luo et al., "Low-loss two-dimensional silicon photonic grating coupler with a backside metal mirror," *Opt. Lett.*, vol. 43, no. 3, pp. 474–477, 2018, doi: [10.1364/OL.43.000474](https://doi.org/10.1364/OL.43.000474).
- [20] Y. Xue, H. Chen, Y. Bao, J. Dong, and X. Zhang, "Two-dimensional silicon photonic grating coupler with low polarization-dependent loss and high tolerance," *Opt. Exp.*, vol. 27, no. 16, pp. 22268–22274, 2019, doi: [10.1364/OE.27.022268](https://doi.org/10.1364/OE.27.022268).
- [21] B. Chen et al., "Two-dimensional grating coupler on silicon with a high coupling efficiency and a low polarization-dependent loss," *Opt. Exp.*, vol. 28, no. 3, pp. 4001–4009, 2020, doi: [10.1364/OE.380338](https://doi.org/10.1364/OE.380338).
- [22] G. Georgieva, K. Voigt, C. Mai, P. M. Seiler, K. Petermann, and L. Zimmermann, "Cross-polarization effects in sheared 2D grating couplers in a photonic BiCMOS technology," *Japanese J. Appl. Phys.*, vol. 59, no. SO, 2020, Art. no. SOOB03, doi: [10.35848/1347-4065/ab8e21](https://doi.org/10.35848/1347-4065/ab8e21).
- [23] G. Georgieva, K. Voigt, P. M. Seiler, C. Mai, K. Petermann, and L. Zimmermann, "A physical origin of cross-polarization and higher-order modes in two-dimensional (2D) grating couplers and the related device performance limitations," *J. Phys.: Photon.*, vol. 3, 2021, Art. no. 035002, doi: [10.1088/2515-7647/ab942](https://doi.org/10.1088/2515-7647/ab942).
- [24] G. Georgieva, P. M. Seiler, C. Mai, K. Petermann, and L. Zimmermann, "2D grating coupler induced polarization crosstalk in coherent transceivers for next generation data center interconnects," in *Proc. Opt. Fiber Commun. Conf.*, 2021, Art. no. W1C.4, doi: [10.1364/OFC.2021.W1C.4](https://doi.org/10.1364/OFC.2021.W1C.4).
- [25] Y. Chen et al., "Modeling and mitigation of polarization crosstalk-induced nonlinearity for the polarization-multiplexed carrier self-homodyne system," *Opt. Lett.*, vol. 47, no. 6, pp. 1423–1426, 2022, doi: [10.1364/OL.450187](https://doi.org/10.1364/OL.450187).
- [26] T. Weiland, "A discretization method for the solution of Maxwell's equations for six-component fields," *Electron. Commun. (AEU)*, vol. 31, pp. 116–120, 1977.
- [27] W. Bogaerts, D. Taillaert, P. Dumon, D. Van Thourhout, R. Baets, and E. Pluk, "A polarization-diversity wavelength duplexer circuit in silicon-on-insulator photonic wires," *Opt. Exp.*, vol. 15, no. 4, pp. 1567–1578, 2007, doi: [10.1364/OE.15.001567](https://doi.org/10.1364/OE.15.001567).
- [28] F. van Laere, W. Bogaerts, P. Dumon, G. Roelkens, D. Van Thourhout, and R. Baets, "Focusing polarization diversity grating couplers in silicon-on-insulator," *J. Lightw. Technol.*, vol. 27, no. 5, pp. 612–618, 2009, doi: [10.1109/JLT.2008.2004946](https://doi.org/10.1109/JLT.2008.2004946).
- [29] J. Zou, Y. Yu, and X. Zhang, "Single step etched two dimensional grating coupler based on the SOI platform," *Opt. Exp.*, vol. 23, no. 25, pp. 32490–32495, 2015, doi: [10.1364/OE.23.032490](https://doi.org/10.1364/OE.23.032490).

- [30] G. Georgieva and K. Petermann, "Analytical and numerical investigation of silicon photonic 2D grating couplers with a waveguide-to-grating shear angle," in *Proc. Prog. Electromagn. Res. Symp.*, 2018, pp. 921–925, doi: [10.23919/PIERS.2018.8598162](https://doi.org/10.23919/PIERS.2018.8598162).
- [31] H. G. Berry, G. Gabrielse, and A. E. Livingston, "Measurement of the stokes parameters of light," *Appl. Opt.*, vol. 16, no. 12, pp. 3200–3205, 1977, doi: [10.1364/AO.16.003200](https://doi.org/10.1364/AO.16.003200).
- [32] F. L. Pedrotti, L. S. Pedrotti, W. Bausch, and H. Schmid, "Matrixbeschreibung der polarisation," in *Optik für Ingenieure*, Heidelberg, Berlin: Springer, 2005, doi: [10.1007/3-540-27379-4_14](https://doi.org/10.1007/3-540-27379-4_14).
- [33] W. Born and E. Wolf, "Basic properties of the electromagnetic field," in *Principles of Optics*, 6th ed. New York, NY, USA: Pergamon Press, 1980.
- [34] C. Delezoide, P. Ramantanis, and P. Layec, "On the performance prediction of optical transmission systems in presence of filtering," in *Proc. 19th Int. Conf. Transparent Opt. Netw.*, 2017, pp. 1–4, doi: [10.1109/IC-TON.2017.8024998](https://doi.org/10.1109/IC-TON.2017.8024998).
- [35] R. Elschner et al., "Experimental demonstration of a format-flexible single-carrier coherent receiver using data-aided digital signal processing," *Opt. Exp.*, vol. 20, no. 27, pp. 28786–28791, 2012, doi: [10.1364/OE.20.028786](https://doi.org/10.1364/OE.20.028786).
- [36] M. Kushnerov et al., "Data-aided versus blind single-carrier coherent receivers," *IEEE Photon. J.*, vol. 2, no. 3, Jun. 2010, doi: [10.1109/JPHOT.2010.2048308](https://doi.org/10.1109/JPHOT.2010.2048308).
- [37] T. Pfau, S. Hoffmann, and R. Noe, "Hardware-efficient coherent digital receiver concept with feedforward carrier recovery for M-QAM constellations," *J. Lightw. Technol.*, vol. 27, no. 8, pp. 989–999, 2009, doi: [10.1109/JLT.2008.2010511](https://doi.org/10.1109/JLT.2008.2010511).
- [38] P. J. Winzer, A. H. Gnauck, A. Konczykowska, F. Jorge, and J.-Y. Dupuy, "Penalties from in-band crosstalk for advanced optical modulation formats," in *Proc. 37th Eur. Conf. Exhib. Opt. Commun.*, 2011, Art. no. Tu.5.B.7, doi: [10.1364/ECOC.2011.Tu.5.B.7](https://doi.org/10.1364/ECOC.2011.Tu.5.B.7).
- [39] P. M. Seiler et al., "Toward coherent O-band data center interconnects," *Front. Optoelectron.*, vol. 14, no. 4, pp. 414–425, 2021, doi: [10.1007/s12200-021-1242-0](https://doi.org/10.1007/s12200-021-1242-0).
- [40] D. Knoll et al., "High-performance photonic BiCMOS process for the fabrication of high-bandwidth electronic-photonic integrated circuits," in *Proc IEEE Int. Electron Devices Meeting*, 2015, pp. 15.6.1–15.6.4, doi: [10.1109/IEDM.2015.7409706](https://doi.org/10.1109/IEDM.2015.7409706).
- [41] D. Knoll et al., "BiCMOS silicon photonics platform for fabrication of high-bandwidth electronic-photonic integrated circuits," in *Proc. IEEE 16th Top. Meeting Silicon Monolithic Integr. Circuits RF Syst.*, 2016, pp. 46–49, doi: [10.1109/SIRF.2016.7445464](https://doi.org/10.1109/SIRF.2016.7445464).